Supporting Information for:

Supersensitive Visual Pressure Sensor Based on the Exciton Luminescence of a Perovskite Material

Marcin Runowski,[1,*] Przemysław Woźny,[1] Kevin Soler-Carracedo,[1] Agata Lazarowska,[2] Mikołaj Kamiński,[2] Natalia Majewska,[2] Alfonso Muñoz,[3] Jan Moszczyński,[1] Szymon Sobczak,[1] Kashyap Dave,[4] Wen-Tse Huang,[4] Ru-Shi Liu,[4] Sebastian Mahlik[2,*]

[1]*Faculty of Chemistry, Adam Mickiewicz University, Uniwersytetu Poznańskiego 8, 61-614 Poznań, Poland*

[2]*Institute of Experimental Physics, Faculty of Mathematics, Physics and Informatics, University of Gdansk, Wita Stwosza 57, 80-308 Gdansk*

[3]*Departamento de Física, IUdEA, IMN & MALTA Consolider Team, Universidad de La Laguna, Apdo. Correos 456, E-38200 San Cristóbal de La Laguna, Santa Cruz de Tenerife, Spain*

[4]*Department of Chemistry, National Taiwan University, Taipei 106, Taiwan*

[*]E-mail: runowski@amu.edu.pl (M.R.); sebastian.mahlik@ug.edu.pl (S.M.)

Table S1. Rietveld refinement results for the synthesized $Cs_2Ag_{0.6}Na_{0.4}In_{0.996}Bi_{0.004}Cl_6$ perovskite.

		$\mathbf{Cs_2Ag_{0.6}Na_{0.4}In_{0.996}Bi_{0.004}Cl_6}$			
Site	***x***	***y***	***z***	***Occ***	***Beq(Å²)***
Cs1	0.25	0.25	0.25	1	1.985(76)
Ag1	0	0	0	0.514(11)	2.22(21)
Na1	0	0	0	0.486(11)	2.22(21)
In1	0.50	0.50	0.50	1.00(59)	1.01(22
Bi1	0.50	0.50	0.50	0.04(37)	1.01(22
Cl1	0.26071(53)	0	0	1	2.08(10)

Table S2. Rietveld refinement results for the synthesized $Cs_2Ag_{0.6}Na_{0.4}In_{0.996}Bi_{0.004}Cl_6$ perovskite.

$\mathbf{Cs_2Ag_{0.6}Na_{0.4}In_{0.996}Bi_{0.004}Cl_6}$	
a (Å)	10.51584(26)
V (Å^3)	1162.874(87)
$Cs_2AgInCl_6$(%)	98.56
AgCl(%)	1.44
χ^2	1.07
R_{wp} (%)	11.10
R_p (%)	7.90

Table S3. Weigh and atomic percentage compositions (with relative errors) of the synthesized material, obtained based on the EDX analysis.

Element	Weight (%)	Atomic (%)	Error (%)
Na	1.88	5.37	12.47
Bi	0.68	0.21	16.07
Cl	32.53	60.35	3.69
Ag	6.41	3.9	5.54
In	15.39	8.82	3.84
Cs	43.11	21.34	2.73

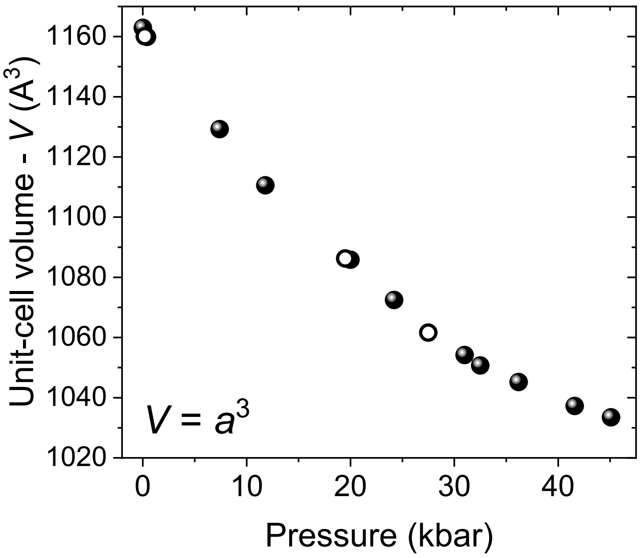

Figure S1. Unit cell volume as a function of pressure, based on the in-situ powder XRD measurements, performed in compression (full symbols) and decompression (empty symbols) cycles for the synthesized $Cs_2Ag_{0.6}Na_{0.4}In_{0.996}Bi_{0.004}Cl_6$ perovskite.

Overview of theoretical studies – DFT calculations

Ab initio calculations within the framework of density functional theory (DFT),[1] as implemented in the Vienna Simulation package (VASP),[2] were performed for the bulk double perovskite $Cs_2AgInCl_6$, i.e., the same structure as the doped material (optimized for luminescence performance) used in this work for high-pressure studies, but without partial occupation. The atomic species used were described by employing the projector-augmented wave pseudopotential (PAW).[3] To obtain highly accurate results, a plane-wave energy cut-off of 400 eV was used. The exchange-correlation energy was described within the generalized gradient approximation (GGA) with the PBE for solids, PBEsol, and prescription.[4] Integrations over the Brillouin zone (BZ) were carried out with (6 × 6 × 6) meshes of Monkhorst-Pack k-points.[5] This procedure allows convergence in energy above 1 meV per formula unit to be achieved. For a set of selected volumes, the cell parameters and atomic positions were fully optimized by calculating the forces on atoms and the stress tensor. In the resulting optimized configurations, the forces on atoms were less than 0.002 eV/Å, and the deviation of the stress tensor components from the diagonal hydrostatic form was lower than 0.1 GPa. Electronic band structure calculations were done by choosing the k-path with the SeeK-path tool. The electronic band structure was studied using the modified Becke-Jhonson (MBJ) meta-GGA functional, which provides similar gap values to those of the hybrid functional group to overcome the well-known DFT underestimation of the band gap energy.[6,7] All the band gap values were rigidly added to the scissor correction of 1.15 eV at every pressure point to match the experimental results.

Lattice-dynamic calculations of the phonon modes were carried out under pressure at the zone center (Γ-point) of the BZ via the direct force-constant approach *via* the Phonopy package.[8] These calculations provide the frequency of the normal modes, their symmetry, and their polarization vectors. The phonon dispersion and the projected phonon density of states (DOS) were obtained with the supercell method employing a (2 × 2 × 2) supercell. The elastic constants were evaluated with the Le Page[9] method implemented in the VASP code to study the mechanical stability and elastic properties of the investigated perovskite material *via* the elastic moduli obtained from the calculated elastic stiffness constants.

Details of the calculation results – DFT studies

The investigated double perovskite belongs to a cubic crystal system, so it has only three independent elastic constants, C_{ij}, at zero pressure, which are related to the abovementioned elastic stiffness coefficient B_{ij} according to the following expression:[10,11]

$$B_{ii} = C_{ii} - P, \text{ for i = 1 to 6} \quad (1)$$

$$B_{ij} = C_{ij} + P, \text{ for } i \neq j \text{ and i, j = 1 to 3} \quad (2)$$

$$B_{ij} = C_{ij}, \text{ for } i \neq j \text{ and i, j = 4 to 6} \quad (3)$$

Notably, a crystal is mechanically stable at zero (ambient) pressure only when the Born stability criteria are fulfilled.[12] In the case of a cubic crystal system, there are three conditions to fulfill:

$$\text{(I) } C_{11} - C_{12} > 0; \text{ (II) } C_{44} > 0; \text{ (III) } C_{11} + 2C_{12} > 0 \quad (4)$$

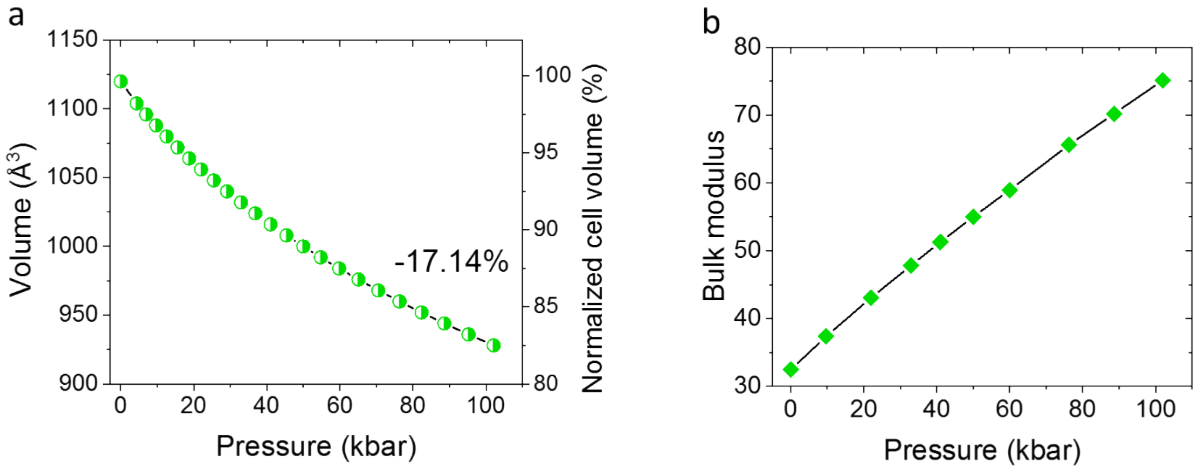

Figure S2. a Simulated (DFT) unit cell volume, and **b** the corresponding bulk modulus as a pressure function for the studied perovskite material.

Table S4. The absolute values of the lattice constants, i.e. unite cell parameter (*a*) and the unit cell volume (*V*) for material under compression process.

Pressure value (kbar)	Unit cell volume, *V* (Å^3)	Lattice parameter *a* = *b* = *c* (Å)
0.001	1120	10.38499
15.5	1072	10.23446
29.1	1040	10.13159
36.8	1024	10.07937
45.4	1008	10.02660
54.7	992	9.97326
65.1	976	9.91935
76.3	960	9.86485
88.6	944	9.80974
102.0	928	9.7540

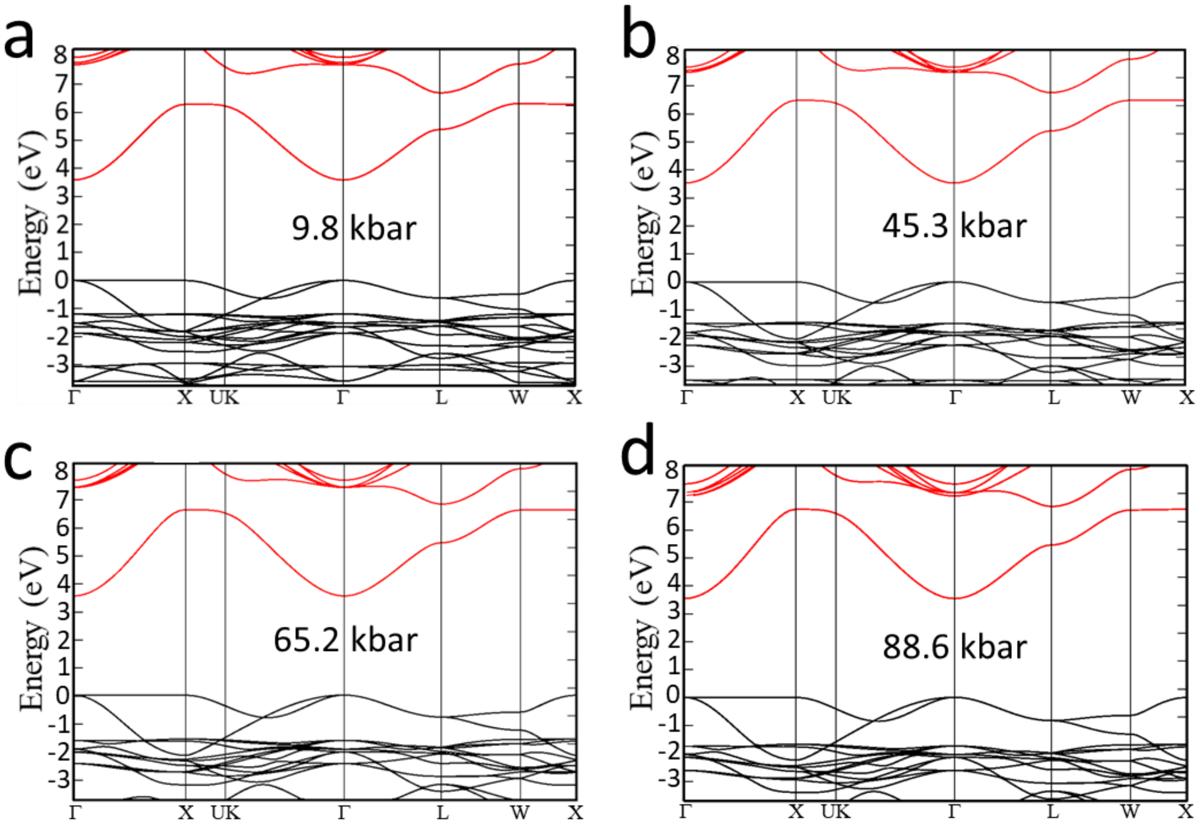

Figure S3. Simulated electronic band structures at 9.8 kbar (a), 45.3 kbar (b), 65.2 kbar (c) and 88.6 kbar (d).

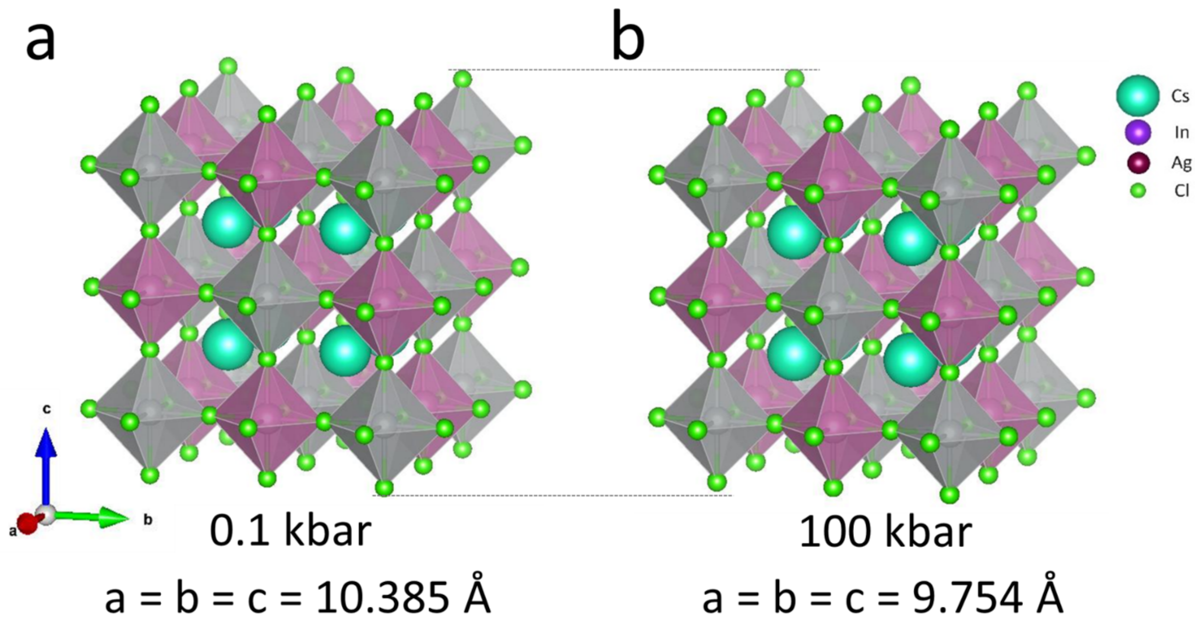

Figure S4. Simulated 3D representations of the investigated perovskite crystal structures at ambient pressure and at 100 kbar.

Table S5. Experimental and simulated (*) Raman modes centroids (energies) at ambient pressure and the corresponding pressure shift rates for the perovskite material studied.

Peak centroid at ambient pressure (cm^{-1})	**Raman mode**	**Shift rate (cm^{-1}/kbar)**
≈ 39*	T_{2g}	0.144
≈ 124*	T_{2g}	0.305
≈ 140	$\mathbf{T_{2g}}$	**0.35**
≈ 151*	E_g	1.16
≈ 275*	A_{1g}	1.05
≈296	$\mathbf{A_{1g}}$	**1.20**

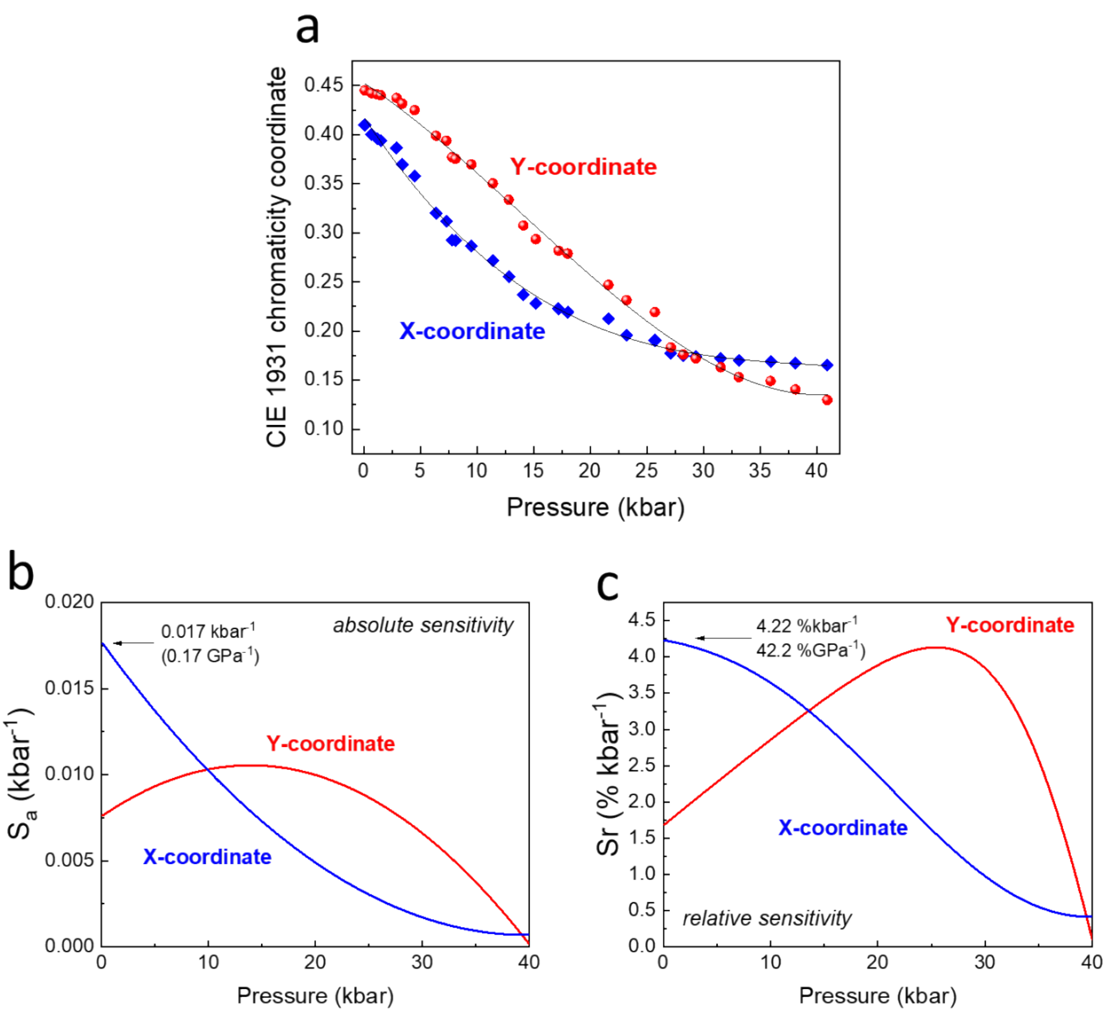

Figure S5. a Determined chromaticity coordinates (Y & X) as a function of pressure. **b** Calculated absolute (Sa) and **c** relative (Sr) pressure sensitivities for the corresponding parameters (Y and X coordinates) as a function of pressure.

Table S6. Comparison of the performances of commonly used and most sensitive optical (luminescent) manometers based on the spectral shift of the emission band.

Compounds	Transition	Operating spectral range	Pressure Sensitivity (nm/GPa)	Temperature dependence (nm/K)	TIMF* parameter	Ref.
$Cs_2Ag_{0.6}Na_{0.4}InCl_6:Bi^{3+}$	Exciton emission	vis	112	0.065	1723	This work
$Li_3Sc_2(PO_4)_3:Cr^{3+}$	$^4T_2 \rightarrow {}^4A_{2g}$	NIR	23.896	0.001	23896	13
$LiScGeO_4:Cr^{3+}$	$^4T_2 \rightarrow {}^4A_{2g}$	NIR	23.63	0.002	11815	14
$[(CH_3)_4\ N_4N]MnCl_3$	$^4T_{1g} \rightarrow {}^6A_{1g}$	vis	21	-	-	15
$BaCN_2:Eu^{2+}$	5d → 4f	vis	19	-	-	16
$Sr_8Si_4O_{12}Cl_8:Eu^{2+}$	5d → 4f	vis	9.69	-	-	17
$NaY_9(SiO_4)_6O_2:Mn^{2+}$	$^4T_1(^4G) \rightarrow {}^6A_1$	vis	7	0.043	163	18
$ZnS/CaZnOS:Mn^{2+}$	$^4T_1 \rightarrow {}^6A_1$	vis	6.2	0.01	620	19
$Ca_9NaZn(PO_4)_7:Eu^{2+}$	5d → 4f	vis	5.21	-	-	20
$Li_4SrCa(SiO_4)_2:Eu^{2+}$	5d → 4f	vis	5.19	-	-	21
$Lu_2Mg_2Al_2Si_2O_{12}:Mn^{2+},Eu^{2+}$	5d → 4f	vis	3.53	-	-	22
$K_2HfSi_2O_7:Eu^{2+}$	5d → 4f	vis	3.25	-	-	23
$Ca_2Gd_8Si_6O_{26}:Ce^{3+}$	5d → 4f	UV-vis	3.00	1.7×10^{-3}	1765	24
$Na_3CsMg_7(PO_4)_6:Eu^{2+}$	5d → 4f	vis	2.13			25
$Mg_2Gd_8(SiO_4)_6O_2:Ce^{3+}$	5d → 4f	vis	1.84			26
$YVO_4:Er^{3+}/Yb^{3+}$	$^4I_{13/2} \rightarrow {}^4I_{15/2}$	NIR	1.766	-5.16×10^{-3}	342	27
$BaLi_2Al_2Si_2N_6:Eu^{2+}$	5d → 4f	vis	1.58	-	-	28
$GdTaO_4:Nd^{3+}$	$^3F_{3/2} \rightarrow {}^4I_{9/2}$ ($R_2 \rightarrow Z_5$)	NIR	1.34	8×10^{-4}	1675	29
$BaFCl:Sm^{2+}$	$^5D_0 \rightarrow {}^7F_0$	vis	1.31	-1.6×10^{-3}	819	30
Y2SiO5:Ge^{4+},Pr^{3+}	5d → 4f	UV	1.28	-	-	31
$Gd_2ZnTiO_6:Mn^{4+}$	$^2E_g \rightarrow {}^4A_{2g}$	vis	1.11	0.012	92	32
$SrFCl:Sm^{2+}$	$^5D_0 \rightarrow {}^7F_0$	vis	1.1	-2.3×10^{-3}	483	33
$Ga_2O_3:Cr^{3+}$	$^2E_g \rightarrow {}^4A_{2g}$ (R_1)	vis	0.948			34
NaBiF4:Er^{3+}	$^4I_{13/2} \rightarrow {}^4I_{15/2}$ (Stark)	NIR	0.8	-	-	35
YPO4:Tm^{3+}	$^3H_4 \rightarrow {}^3H_6$	NIR	0.8	$\approx 3 \times 10^{-3}$	267	36
$YAlO_3:Cr^{3+}$	$^2E \rightarrow {}^4A_2$	vis	0.70	7.6×10^{-3}	92	37
$Gd_3Sc_2Ga_3O_{12}:Nd^{3+}$	$^4F_{3/2} \rightarrow {}^4I_{9/2}$ (Stark)	NIR	~0.632	-	-	38
$Y_6Ba_4(SiO_4)_6F_2:Ce^{3+}$	5d → 4f	vis	0.63	-	-	39

$YPO_4:Er^{3+}$	$^4I_{13/2}\rightarrow{}^4I_{15/2}$ (Stark)	NIR	0.539	-1.78×10^{-3}	303	40
$MgO:Cr^{3+}$	$^2E_g \rightarrow {}^4A_{2g}$	vis	0.504	-	-	41
Al_2O_3(ruby): Cr^{3+}	$^2E\rightarrow{}^4A_2$	vis	0.365	7×10^{-3}	52	42
$Y_3Al_5O_{12}:Sm^{2+}$	$^4G_{5/2}\rightarrow{}^6H_{7/2}$ (Stark)	vis	0.3	2.3×10^{-4}	1304	43
CeN-PVDF (Ce^{3+})	5d → 4f	UV	0.28	-	-	44
$EuPO_4$	$^5D_0 \rightarrow {}^7F_0$	vis	0.27	-	-	45
$SrB_4O_7:Sm^{2+}$	$^5D_0 \rightarrow {}^7F_0$	vis	0.255	-1×10^{-4}	2550	46
$SrB_2O_4:Sm^{2+}$	$^5D_0 \rightarrow {}^7F_0$	vis	0.24	-1×10^{-4}	2400	47
Y3Al5O12:Eu3+			0.197			
$YF_3:Er^{3+}$	$^4F_{9/2}\rightarrow{}^4I_{15/2}$ (Stark)	vis	0.186	-3×10^{-4}	618	48
SrB4O7:Eu2+	$^6P_{7/2}\rightarrow{}^8S_{7/2}$	UV	0.17	4.8×10^{-4}	354	49
YAlO3:Nd3+	$^4F_{3/2}\rightarrow{}^4I_{9/2}$ (Stark)	NIR	0.13	1×10^{-3}	130	37
KMgF3:Eu2+	$^6P_{7/2}\rightarrow{}^8S_{7/2}$	UV	0.13	-	-	50

**TIMF* = temperature invariant manometric factor. In order to quantitatively asses the effect of temperature on the pressure sensing performance, the TIMF paramater has been introduced recently, which can be calculated as follows:

$$\text{TIMF} = \frac{\text{sensitivity(p)}}{\text{sensitivity(T)}} \quad (5)$$

where *sensitivity(p)* is the maximum pressure sensitivity (per 1 GPa) and *sensitivity(T)* is the temperature sensitivity (per 1 K) at ambient conditions. In general, the TIMF factors higher than 100 characterize the pressure sensors which can properly work under variable temperature conditions, providing reliable pressure readouts.

Table S7. Comparison of the performances of commonly used and most sensitive optical (luminescent) manometers based on the emission bandwidth (FWHM).

Compounds	Transition	Operating spectral range	Pressure Sensitivity (nm/GPa)	Temperature dependence (nm/K)	TIMF parameter	Ref.
$Cs_2Ag_{0.6}Na_{0.4}InCl_6:Bi^{3+}$	Exciton emission	vis	31.5	0.2547	124	This work
$NaY_9(SiO_4)_6O_2:Mn^{2+}$	$^4T_1(^4G) \rightarrow {}^6A_1$	vis	10.13	0.083	122	18
$Ca_2Gd_8Si_6O_{26}:Ce^{3+}$	5d → 4f	UVvis	2.45	2.3×10^{-3}	1065	24
$Y_6Ba_4(SiO_4)_6F_2:Ce^{3+}$	5d → 4f	vis	~1.81	-	-	39

$Li_4SrCa(SiO_4)_2:Eu^{2+}$	5d → 4f	vis	1.23	-	-	[21]
$SrB_4O_7:Tm^{2+}$	5d → 4f	vis	0.89	0.053	17	[51]
$Y_2Hf_2O_7$	$^5D_0 \rightarrow ^7F_2$	vis	0.53	-	-	[52]
$NaBiF_4:Er^{3+}$	$^4F_{9/2} \rightarrow ^4I_{15/2}$	NIR	0.23	-	-	[35]

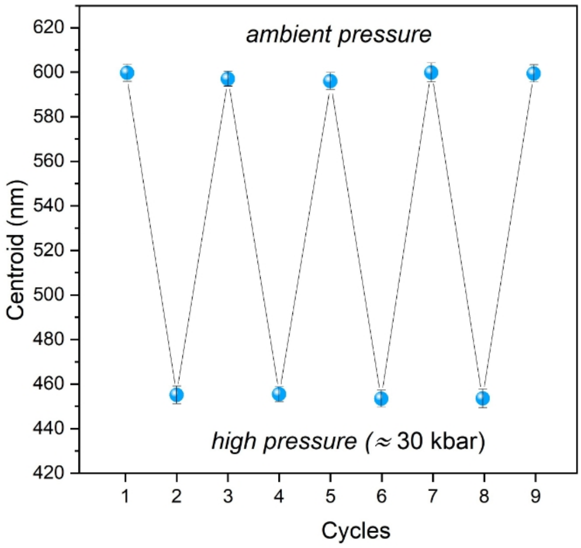

Figure S6. Pressure cycling data for the developed perovskite sensor - evolution of its emission band centroid (manometric parameter) during the material compression and pressure release, by cycling the sample between the extreme pressure values, i.e. ambient and high-pressure conditions (≈30 kbar).

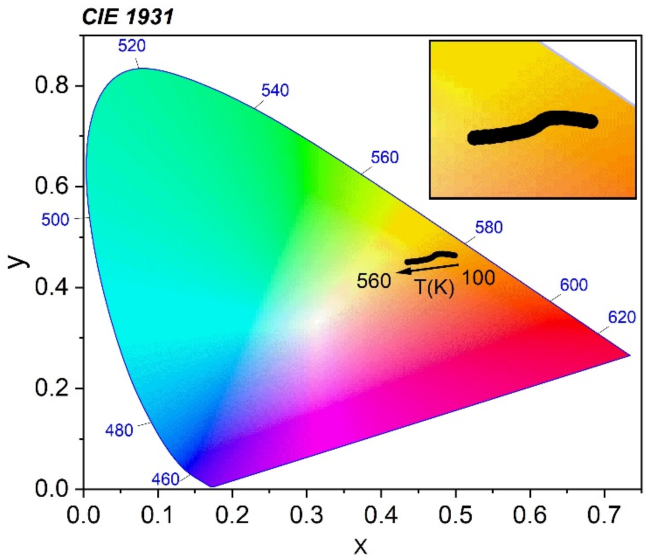

Figure S7. CIE (1931) color diagram showing the thermal evolution of the *x* and *y* color coordinates, determined based on the recorded emission spectra.

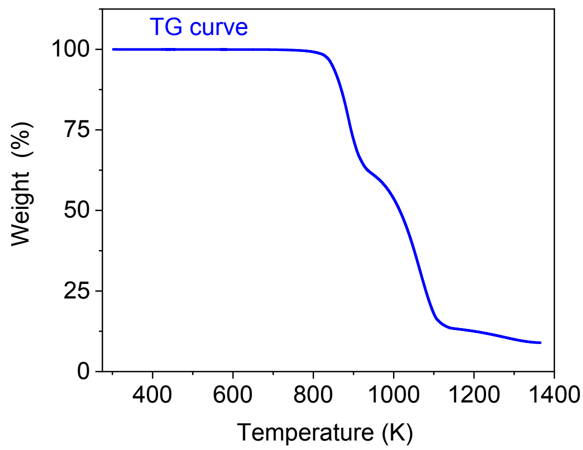

Figure S8. Termogravimetric (TG) curve from 300 to 1373 K for the $Cs_2Ag_{0.6}Na_{0.4}In_{0.996}Bi_{0.004}Cl_6$ sample.

Uniaxial pressure experiments

In this experiment, we applied relatively low forces ranging from ca. 20 to 425 N, corresponding to approximately 25-600 bar pressure values. The adjustment of the force/pressure in the system studied was based on the use of different weights on the sample surface, corresponding to the given mass acting on the confined material volume. The values of the applied force and pressure can be calculated based on the well-known relationships between the fundamental physical quantities, where the gravitational force exerted by an object is given by $F = m \times g$ (where F is the force in Newtons, m is the mass in kilograms, g is the acceleration due to gravity, 9.81 m/s) and $p = F/S$ (where S is the surface area). For the first series of experiments, we used pure perovskite powder material. We conducted four different compression cycles, differing in the amount of the loading sample (1.51-3.74 mg) placed between two identical, circular quartz plates (3 mm^2 in diameter) located in a measuring chamber. As expected for the uniaxial pressure experiments (in contrast to the isostatic measurements in a DAC), the amount of material studied affects the spectral position of the emission band centroid, so the observed shift rate during compression increases (Figure 6b). This is because when squeezing a small quantity of the sample, which forms a thin layer that is non-uniformly deposited on the surface of the measuring chamber, the resulting contact area is smaller than that of the quartz plates used, further producing higher force/pressure than the expected value. On the other hand, the opposite effect can be observed for larger amounts of sample, i.e., exceeding the required amount of material to form a perfect, thin layer on the contact surface. In such a case, the contact pressure should be the same as that calculated from the first principles; however, it entirely acts only on the sample surface, i.e., the interface between the material and the contact object (quartz), whereas the whole volume of the material is subjected to an average pressure that is lower than the value calculated for the isostatic conditions.

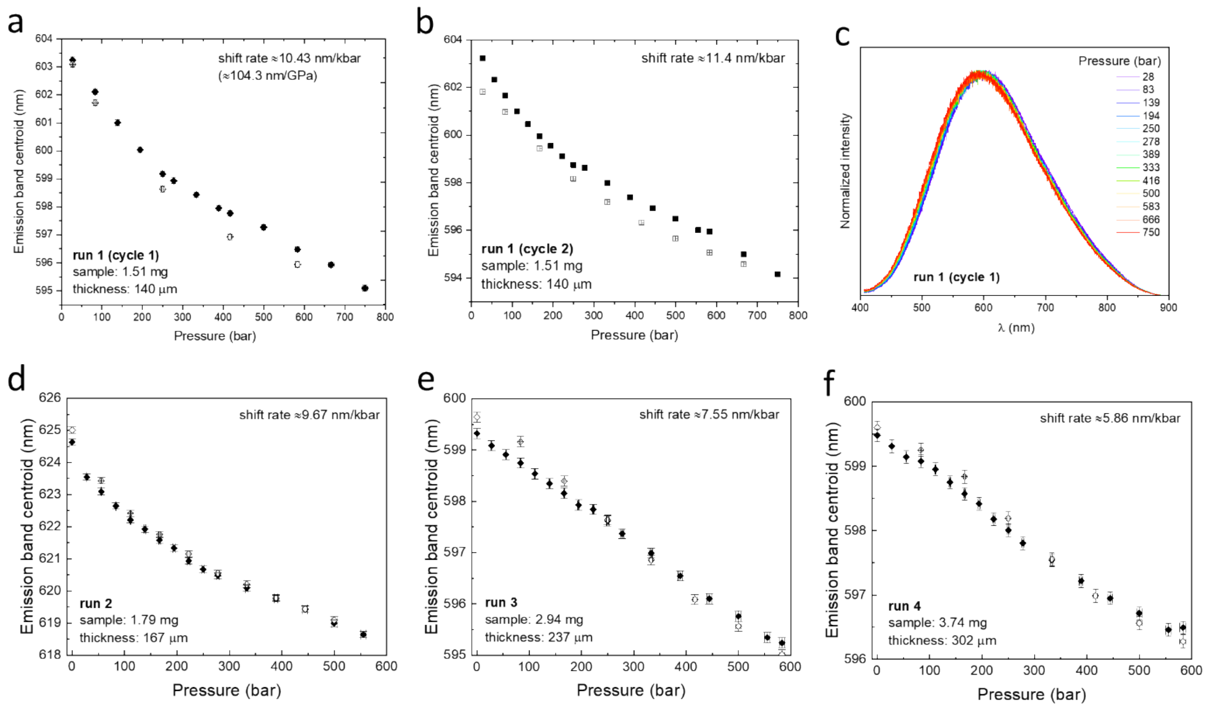

Figure S9. a-b, Emission band centroids of the developed perovskite sensor as a function of uniaxial pressure determined in run 1, for two repetitive cycles (1 – **a**; 2 – **b**) of single loading, with sample mass of 1.51 mg, and 140 μm thick. **c**, Representative emission spectra measured at different uniaxial pressure values for run 1, cycle 1. **d-f**, Emission band centroids of the developed perovskite sensor as a function of uniaxial pressure determined in three repetitive sample loadings, i.e., run 2 (**d**, sample mass: 1.79 mg; thickness: 167 μm), run 3 (**e**, 2.94 mg; 237 μm) and run 4 (**f**, 3.74 mg; 302 μm); λ_{ex} = 375 nm.

References

(1) Hohenberg, P.; Kohn, W. Inhomogeneous Electron Gas. *Phys. Rev.* **1964**, *136* (3B), B864–B871. https://doi.org/10.1103/PhysRev.136.B864.

(2) Kresse, G.; Furthmüller, J. Efficiency of Ab-Initio Total Energy Calculations for Metals and Semiconductors Using a Plane-Wave Basis Set. *Comput. Mater. Sci.* **1996**, *6* (1), 15–50. https://doi.org/10.1016/0927-0256(96)00008-0.

(3) Blöchl, P. E. Projector Augmented-Wave Method. *Phys. Rev. B* **1994**, *50* (24), 17953–17979. https://doi.org/10.1103/PhysRevB.50.17953.

(4) Perdew, J. P.; Ruzsinszky, A.; Csonka, G. I.; Vydrov, O. A.; Scuseria, G. E.; Constantin, L. A.; Zhou, X.; Burke, K. Restoring the Density-Gradient Expansion for Exchange in Solids and Surfaces. *Phys. Rev. Lett.* **2008**, *100* (13), 136406.

https://doi.org/10.1103/PhysRevLett.100.136406.

(5) Hu, K.; Wu, M.; Hinokuma, S.; Ohto, T.; Wakisaka, M.; Fujita, J.; Ito, Y. Boosting Electrochemical Water Splitting via Ternary NiMoCo Hybrid Nanowire Arrays. *J. Mater. Chem. A* **2019**, *7* (5), 2156–2164. https://doi.org/10.1039/C8TA11250A.

(6) Becke, A. D.; Johnson, E. R. A Simple Effective Potential for Exchange. *J. Chem. Phys.* **2006**, *124* (22), 221101. https://doi.org/10.1063/1.2213970.

(7) Tran, F.; Blaha, P. Accurate Band Gaps of Semiconductors and Insulators with a Semilocal Exchange-Correlation Potential. *Phys. Rev. Lett.* **2009**, *102* (22), 226401. https://doi.org/10.1103/PhysRevLett.102.226401.

(8) Togo, A.; Tanaka, I. First Principles Phonon Calculations in Materials Science. *Scr. Mater.* **2015**, *108*, 1–5. https://doi.org/10.1016/j.scriptamat.2015.07.021.

(9) Le Page, Y.; Saxe, P. Symmetry-General Least-Squares Extraction of Elastic Data for Strained Materials from Ab Initio Calculations of Stress. *Phys. Rev. B* **2002**, *65* (10), 104104. https://doi.org/10.1103/PhysRevB.65.104104.

(10) Wallace, D. C.; Callen, H. Thermodynamics of Crystals. *Am. J. Phys.* **1972**, *40* (11), 1718–1719. https://doi.org/10.1119/1.1987046.

(11) Grimvall, G.; Magyari-Köpe, B.; Ozoliņš, V.; Persson, K. A. Lattice Instabilities in Metallic Elements. *Rev. Mod. Phys.* **2012**, *84* (2), 945–986. https://doi.org/10.1103/RevModPhys.84.945.

(12) Born, M.; Huang, K.; Lax, M. Dynamical Theory of Crystal Lattices. *Am. J. Phys.* **1955**, *23* (7), 474–474. https://doi.org/10.1119/1.1934059.

(13) Szymczak, M.; Jaśkielewicz, J.; Runowski, M.; Xue, J.; Mahlik, S.; Marciniak, L. Highly-Sensitive, Tri-Modal Luminescent Manometer Utilizing Band-Shift, Ratiometric and Lifetime-Based Sensing Parameters. *Adv. Funct. Mater.* **2024**, 2314068. https://doi.org/10.1002/adfm.202314068.

(14) Szymczak, M.; M.Runowski; Brik, M. G.; Marciniak, L. Multimodal, Supersensitive Luminescent Manometer Based on Giant Pressure-Induced Spectral Shift of Cr3+ in the NIR Range. *Chem. Eng. J.* **2023**, *466* (February), 143130. https://doi.org/10.1016/j.cej.2023.143130.

(15) Nataf, L.; Rodríguez, F.; Valiente, R.; González, J. Spectroscopic and Luminescence Properties of (CH 3) 4 NMnCl 3□: A Sensitive Mn 2+ -Based Pressure Gauge. *High Press. Res.* **2009**, *29* (4), 653–659. https://doi.org/10.1080/08957950903414979.

(16) Masubuchi, Y.; Nishitani, S.; Miyazaki, S.; Hua, H.; Ueda, J.; Higuchi, M.; Tanabe, S. Large Red-Shift of Luminescence from BaCN 2□:Eu 2+ Red Phosphor under High Pressure. *Appl. Phys. Express* **2020**, *13* (4), 042009. https://doi.org/10.35848/1882-0786/ab8055.

(17) Zheng, T.; Runowski, M.; Xue, J.; Luo, L.; Rodríguez-Mendoza, U. R.; Lavín, V.; Martín, I. R.; Rodríguez-Hernández, P.; Muñoz, A.; Du, P. Giant Pressure-Induced Spectral Shift in Cyan-Emitting Eu 2+ -Activated Sr 8 Si 4 O 12 Cl 8 Microspheres for Ultrasensitive Visual Manometry. *Adv. Funct. Mater.* **2023**, *33* (26), 2214663. https://doi.org/10.1002/adfm.202214663.

(18) Zeng, Q.; Runowski, M.; Xue, J.; Luo, L.; Marciniak, L.; Lavín, V.; Du, P. Pressure-Induced Remarkable Spectral Red-Shift in Mn 2+ -Activated NaY 9 (SiO 4) 6 O 2 Red-Emitting Phosphors for High-Sensitive Optical Manometry. *Adv. Sci.* **2023**, 2308221. https://doi.org/10.1002/advs.202308221.

(19) Zheng, T.; Runowski, M.; Martín, I. R.; Soler-Carracedo, K.; Peng, L.; Skwierczyńska, M.;

Sójka, M.; Barzowska, J.; Mahlik, S.; Hemmerich, H.; et al. Mechanoluminescence and Photoluminescence Heterojunction for Superior Multimode Sensing Platform of Friction, Force, Pressure, and Temperature in Fibers and 3D-Printed Polymers. *Adv. Mater.* **2023**, *35* (40), 2304140. https://doi.org/10.1002/adma.202304140.

(20) Zhang, D.; Zheng, B.; Zheng, Z.; Li, L.; Yang, Q.; Song, Y.; Zou, B.; Zou, H. Multifunctional Ca9NaZn1-YMgy(PO4)7:Eu2+ Phosphor for Full-Spectrum Lighting, Optical Thermometry and Pressure Sensor Applications. *Chem. Eng. J.* **2022**, *431* (P1), 133805. https://doi.org/10.1016/j.cej.2021.133805.

(21) Su, K.; Mei, L.; Guo, Q.; Shuai, P.; Wang, Y.; Liu, Y.; Jin, Y.; Peng, Z.; Zou, B.; Liao, L. Multi-Mode Optical Manometry Based on Li 4 SrCa(SiO 4) 2:Eu 2+ Phosphors. *Adv. Funct. Mater.* **2023**, *33* (49), 2305359. https://doi.org/10.1002/adfm.202305359.

(22) Zheng, Z.; Song, Y.; Zheng, B.; Zhao, Y.; Wang, Q.; Zhang, X.; Zou, B.; Zou, H. Eu 2+ and Mn 2+ Co-Doped Lu 2 Mg 2 Al 2 Si 2 O 12 Phosphors for High Sensitivity and Multi-Mode Optical Pressure Sensing. *Inorg. Chem. Front.* **2023**, *10* (9), 2788–2798. https://doi.org/10.1039/D3QI00198A.

(23) Lv, Q.; Wang, C.; Chen, S.; Zheng, H.; Dong, E.; Zhu, G. Ultrasensitive Pressure-Induced Optical Materials: Europium-Doped Hafnium Silicates with a Khibinskite Structure for Optical Pressure Sensors and WLEDs. *Inorg. Chem.* **2022**, *61* (7), 3212–3222. https://doi.org/10.1021/acs.inorgchem.1c03674.

(24) Zheng, T.; Luo, L.; Du, P.; Lis, S.; Rodríguez-Mendoza, U. R.; Lavín, V.; Martín, I. R.; Runowski, M. Pressure-Triggered Enormous Redshift and Enhanced Emission in Ca2Gd8Si6O26:Ce3+ Phosphors: Ultrasensitive, Thermally-Stable and Ultrafast Response Pressure Monitoring. *Chem. Eng. J.* **2022**, *443* (February), 136414. https://doi.org/10.1016/j.cej.2022.136414.

(25) Chen, H.; Seto, T.; Wang, Y. An Efficient Blue Phosphor with High Thermal Stability for Lighting and Optical Pressure Sensor Applications. *Inorg. Chem. Front.* **2022**, *9* (8), 1644–1654. https://doi.org/10.1039/D2QI00025C.

(26) Zheng, B.; Zhang, X.; Zhang, D.; Wang, F.; Zheng, Z.; Yang, X.; Yang, Q.; Song, Y.; Zou, B.; Zou, H. Ultra-Wideband Phosphor Mg2Gd8(SiO4)6O2:Ce3+,Mn2+: Energy Transfer and Pressure-Driven Color Tuning for Potential Applications in LEDs and Pressure Sensors. *Chem. Eng. J.* **2022**, *427*, 131897. https://doi.org/10.1016/j.cej.2021.131897.

(27) Runowski, M.; Zheng, T.; Woźny, P.; Du, P. NIR Emission of Lanthanides for Ultrasensitive Luminescence Manometry—Er 3+ -Activated Optical Sensor of High Pressure. *Dalt. Trans.* **2021**, *50* (41), 14864–14871. https://doi.org/10.1039/D1DT02681J.

(28) Wang, Y.; Seto, T.; Ishigaki, K.; Uwatoko, Y.; Xiao, G.; Zou, B.; Li, G.; Tang, Z.; Li, Z.; Wang, Y. Pressure-Driven Eu 2+ -Doped BaLi 2 Al 2 Si 2 N 6: A New Color Tunable Narrow-Band Emission Phosphor for Spectroscopy and Pressure Sensor Applications. *Adv. Funct. Mater.* **2020**, *30* (34), 2001384. https://doi.org/10.1002/adfm.202001384.

(29) Zhou, P.; Zhang, Q.; Peng, F.; Sun, B.; Dou, X.; Liu, B.; Han, D.; Xue, Y.; Ding, K. Optical Properties of Nd3+ Ions Doped GdTaO4 for Pressure and Temperature Sensing. *J. Rare Earths* **2022**, *40* (6), 870–877. https://doi.org/10.1016/j.jre.2021.04.003.

(30) Comodi, P.; Zanazzi, P. F. Improved Calibtration Curve for the Sm 2+:BaFCl Pressure Sensor. *J. Appl. Crystallogr.* **1993**, *26* (6), 843–845. https://doi.org/10.1107/S0021889893006120.

(31) Sójka, M.; Runowski, M.; Woźny, P.; Carlos, L. D.; Zych, E.; Lis, S. Y 2 (Ge,Si)O 5:Pr Phosphors: Multimodal Temperature and Pressure Sensors Shaped by Bandgap Management. *J. Mater. Chem. C* **2021**, *9* (39), 13818–13831. https://doi.org/10.1039/D1TC03202J.

(32) Zheng, T.; Luo, L.; Du, P.; Lis, S.; Rodríguez-Mendoza, U. R.; Lavín, V.; Runowski, M. Highly-Efficient Double Perovskite Mn4+-Activated Gd2ZnTiO6 Phosphors: A Bifunctional Optical Sensing Platform for Luminescence Thermometry and Manometry. *Chem. Eng. J.* **2022**, *446* (P1), 136839. https://doi.org/10.1016/j.cej.2022.136839.

(33) Lorenz, B.; Shen, Y. R.; Holzapfel, W. B. Characterization of the New Luminescence Pressure Sensor SrFCl:Sm 2+. *High Press. Res.* **1994**, *12* (2), 91–99. https://doi.org/10.1080/08957959408203170.

(34) P Beales, T.; H L Goodman, C.; Scarrott, K. A New High Pressure Calibrant: β-Ga2O3:Cr. *Solid State Commun.* **1990**, *73* (1), 1–3. https://doi.org/10.1016/0038-1098(90)90002-S.

(35) Antoniak, M. A.; Zelewski, S. J.; Oliva, R.; Żak, A.; Kudrawiec, R.; Nyk, M. Combined Temperature and Pressure Sensing Using Luminescent NaBiF 4□:Yb,Er Nanoparticles. *ACS Appl. Nano Mater.* **2020**, *3* (5), 4209–4217. https://doi.org/10.1021/acsanm.0c00403.

(36) Runowski, M.; Shyichuk, A.; Tymiński, A.; Grzyb, T.; Lavín, V.; Lis, S. Multifunctional Optical Sensors for Nanomanometry and Nanothermometry: High-Pressure and High-Temperature Upconversion Luminescence of Lanthanide-Doped Phosphates—LaPO 4 /YPO 4□:Yb 3+ –Tm 3+. *ACS Appl. Mater. Interfaces* **2018**, *10* (20), 17269–17279. https://doi.org/10.1021/acsami.8b02853.

(37) Barnett, J. D.; Block, S.; Piermarini, G. J. An Optical Fluorescence System for Quantitative Pressure Measurement in the Diamond-Anvil Cell. *Rev. Sci. Instrum.* **1973**, *44* (1), 1–9. https://doi.org/10.1063/1.1685943.

(38) León-Luis, S. F.; Muñoz-Santiuste, J. E.; Lavín, V.; Rodríguez-Mendoza, U. R. Optical Pressure and Temperature Sensor Based on the Luminescence Properties of Nd^3+ Ion in a Gadolinium Scandium Gallium Garnet Crystal. *Opt. Express* **2012**, *20* (9), 10393. https://doi.org/10.1364/OE.20.010393.

(39) Runowski, M.; Woźny, P.; Stopikowska, N.; Guo, Q.; Lis, S. Optical Pressure Sensor Based on the Emission and Excitation Band Width (Fwhm) and Luminescence Shift of Ce 3+ -Doped Fluorapatite—High-Pressure Sensing. *ACS Appl. Mater. Interfaces* **2019**, *11* (4), 4131–4138. https://doi.org/10.1021/acsami.8b19500.

(40) Runowski, M.; Woźny, P.; Martín, I. R. Optical Pressure Sensing in Vacuum and High-Pressure Ranges Using Lanthanide-Based Luminescent Thermometer–Manometer. *J. Mater. Chem. C* **2021**, *9* (13), 4643–4651. https://doi.org/10.1039/D1TC00709B.

(41) Szymczak, M.; Runowski, M.; Lavín, V.; Marciniak, L. Highly Pressure-Sensitive, Temperature Independent Luminescence Ratiometric Manometer Based on MgO:Cr 3+ Nanoparticles. *Laser Photon. Rev.* **2023**, *17* (4), 2200801. https://doi.org/10.1002/lpor.202200801.

(42) Mao, H. K.; Xu, J.; Bell, P. M. Calibration of the Ruby Pressure Gauge to 800 Kbar under Quasi-Hydrostatic Conditions. *J. Geophys. Res.* **1986**, *91* (B5), 4673–4676. https://doi.org/10.1029/JB091iB05p04673.

(43) Hess, N. J.; Exarhos, G. J. Temperature and Pressure Dependence of Laser Induced Fluorescence in Sm:YAG—a New Pressure Calibrant. *High Press. Res.* **1989**, *2* (1), 57–64. https://doi.org/10.1080/08957958908201032.

(44) Hernandez, C.; Gupta, S. K.; Zuniga, J. P.; Vidal, J.; Galvan, R.; Martinez, M.; Guzman, H.; Chavez, L.; Mao, Y.; Lozano, K. Performance Evaluation of Ce3+ Doped Flexible PVDF Fibers for Efficient Optical Pressure Sensors. *Sensors Actuators A Phys.* **2019**, *298*, 111595. https://doi.org/10.1016/j.sna.2019.111595.

(45) Chen, G.; Hölsä, J.; Peterson, J. R. A Luminescence Study of Single-Crystal EuPO4 at High Pressure. *J. Phys. Chem. Solids* **1997**, *58* (12), 2031–2037. https://doi.org/10.1016/S0022-

3697(97)00133-9.

(46) Datchi, F.; LeToullec, R.; Loubeyre, P. Improved Calibration of the SrB 4 O 7: Sm 2+ Optical Pressure Gauge: Advantages at Very High Pressures and High Temperatures. *J. Appl. Phys.* **1997**, *81* (April), 3333–3339. https://doi.org/10.1063/1.365025.

(47) Runowski, M.; Woźny, P.; Lavín, V.; Lis, S. Optical Pressure Nano-Sensor Based on Lanthanide Doped SrB2O4:Sm2+ Luminescence – Novel High-Pressure Nanomanometer. *Sensors Actuators B Chem.* **2018**, *273* (March), 585–591. https://doi.org/10.1016/j.snb.2018.06.089.

(48) Goderski, S.; Runowski, M.; Woźny, P.; Lavín, V.; Lis, S. Lanthanide Upconverted Luminescence for Simultaneous Contactless Optical Thermometry and Manometry–Sensing under Extreme Conditions of Pressure and Temperature. *ACS Appl. Mater. Interfaces* **2020**, *12* (36), 40475–40485. https://doi.org/10.1021/acsami.0c09882.

(49) Zheng, T.; Runowski, M.; Rodríguez-Hernández, P.; Muñoz, A.; Manjón, F. J.; Sójka, M.; Suta, M.; Zych, E.; Lis, S.; Lavín, V. Pressure-Driven Configurational Crossover between 4f7 and 4f65d1 States – Giant Enhancement of Narrow Eu2+ UV-Emission Lines in SrB4O7 for Luminescence Manometry. *Acta Mater.* **2022**, *231*, 117886. https://doi.org/10.1016/j.actamat.2022.117886.

(50) Barzowska, J.; Lesniewski, T.; Mahlik, S.; Seo, H. J.; Grinberg, M. KMgF3:Eu2+ as a New Fluorescence-Based Pressure Sensor for Diamond Anvil Cell Experiments. *Opt. Mater. (Amst).* **2018**, *84* (January), 99–102. https://doi.org/10.1016/j.optmat.2018.06.057.

(51) Zheng, T.; Sójka, M.; Runowski, M.; Woźny, P.; Lis, S.; Zych, E. Tm 2+ Activated SrB 4 O 7 Bifunctional Sensor of Temperature and Pressure—Highly Sensitive, Multi-Parameter Luminescence Thermometry and Manometry. *Adv. Opt. Mater.* **2021**, *9* (22), 2101507. https://doi.org/10.1002/adom.202101507.

(52) Gupta, S. K.; Mao, Y. High Pressure Induced Disappearing 5D0 → 7F2 and Broadening 5D0 → 7F1 Transitions from Y2Hf2O7:Eu3+ Nanoparticles. *Mater. Lett.* **2021**, *303*, 130560. https://doi.org/https://doi.org/10.1016/j.matlet.2021.130560.